Elastic properties of iron-based superconductor $Ba(Fe_{1-x}Co_x)_2As_2$ and related materials

鉄系超伝導体 $Ba(Fe_{1-x}Co_x)_2As_2$ と関連物質の弾性的性質に関する研究

2013 年 9 月

岩手大学工学研究科
フロンティア物質機能工学専攻

SHALAMUJIANG SIMAYI

Acknowledgments

It is my great pleasure to express my gratitude to the following people for their help concerning my study.

First of all, I would like to express my sincere gratitude to my supervisor Prof. Masahito Yoshizawa for guiding me to the exciting and fruitful research project and continuous encouragement throughout my study. His guidance and patience helped me go through in those unproductive days. Without Prof. Yoshizawa's continuous efforts and supports, this thesis is simply impossible.

I have been very fortunate to work with Dr. Yoshiki Nakanishi. He not only educated me with his knowledge, but also shared with me his brilliant ideas. The conversation with him made me understand Japanese culture and Japanese life style.

I would like to thank to Mr Nakamura, who always helped to any technical problem during the experiment, and helped a lot making the experimental devices.

Thanks are also due to Mr Ikeda, who helped me a lot about the problems in the laboratory. I really hope Mr. Ikeda will come back again to Yoshizawa group. I would like to thank all the former and current members of Yoshizawa group: Mr. Kohei Sakanoa, Mr. Haruka Takezawa, Miss Qiaki Fuji for their a lot of experimental support, and teaching Japanese at the free time.

I would like to thank Kunihiro Kihou, Chul-Ho Lee, Akira Iyo, Hiroshi

Eisaki, who from the "National Institute of Advanced Industrial Science and Technology (AIST), Tsukuba", Masamichi Nakajima, and Shin-ichi Uchida, who from the The University of Tokyo, for supplying the high-quality single crystals of $Ba(Fe_{1-x}Co_x)_2As_2$. I would like to thank again Dr. $\bar{O}$nuki and Dr. Settai from Osaka University for supplying the high-quality single crystals of $Rh_{17}S_{15}$.

Abstract

The discovery of superconductivity in $LaFeAsO_{1-x}F_x$ with the transition temperature of $T_{sc} = 26$ K, puts the iron pnictide superconductors in the first stage of the experimental and theoretical studies in superconducting research. The discovery of iron-based superconductors with high phase transition temperature was unexpected, because it contains a magnetic element Fe, for this reason it has opened a new avenue of research so far. Main discussion in this system now is focused on the mechanism of the superconductivity. In this thesis we have studied the elastic constant properties of $Ba(Fe_{1-x}Co_x)_2As_2$. The parent compound of this material shows a stripe magnetic order with a structural change from tetragonal to orthorhombic. This work mainly discuss the roles and relations of the structural and magnetic fluctuation of this system.

The thesis is organized as follows. We will first provide the necessary background knowledge of the iron-based superconductors in Chapter 1. Chapter 2 serves as various experimental methods and their apparatus for elastic constants, electrical resistivity, heat capacity measurements. In chapter 3, we will show the experimental results of all elastic constants, electrical resistivity, heat capacity. In chapter 4, we discussed the large elastic softening in C_{66} towards to the structural phase transition temperature. We analyzed the origin of the large elastic softening in C_{66} based on localized picture and based on band picture and find some

parameters and summarized the phase diagram of $Ba(Fe_{1-x}Co_x)_2As_2$. At last we discussed the correlation between elastic anomaly and superconductivity in iron based superconductor $Ba(Fe_{1-x}Co_x)_2As_2$, and revealed the role of orbital in the emergence of superconductivity in iron-based superconductors. In chapter 5, we focused our attention on the three-dimensional character of this system. In our experimental tool, ultrasonic measurement, the corresponding elastic strain modulates physical quantities along c-axis through the elongation and contraction of the inter-layer spacing. So by examining the corresponding elastic constant C_{33}, we can obtain the three-dimensional character of this system. Our studies show that the correlation of C_{33} with T_{sc} as well as the in-plane fluctuation appearing in C_{66}.

In chapter 6 we will demonstrate the large elastic anomalies in heavy fermion superconductor $Rh_{17}S_{15}$. In this chapter we summarized the introduction, experimental method, results and discussion in individual. In this chapter we will show the elastic constants of C_{11}, C_{44}, $C_L = \frac{1}{2}(C_{11} + C_{12} + 2C_{44})$, $C_E = \frac{1}{2}(C_{11} - C_{12})$ and discuss the similarities with the iron-based superconductors. is the main contents of the thesis. In this chapter we will demonstrate the existence of the inter-layer fluctuation and the highlight the roles of the magnetic fluctuation. In chapter 7, we will conclude our results of ultrasonic measurements of $Ba(Fe_{1-x}Co_x)_2As_2$. Chapter 8 is Appendix for the analyzing of the elastic constants.

Contents

Chapter 1

Back ground

1.1 Discovery of iron based superconductivity

The discovery of superconductivity in $LaFeAsO_{1-x}F_x$ with the transition temperature of $T_{sc} = 26$ K by Hosono group in 2008 [1] puts the iron pnictide superconductors in the first stage of the experimentation and theoretical studies in superconducting research. With the achieving of many researchers for their high T_{sc} and superconductivity emerges in the system with the ferromagnetic Fe element, many new superconducting materials were discovered so far [2, 3, 5, 6, 7, 8].

In a very short time, the superconducting transition temperature T_{sc} was raised to around 55 K [6], which is only second to that of the copper-oxide superconductors. Except for the first iron based superconductor material so-called 1111 family, new families of the iron-based superconductors were also discovered one after another. To date, five unique crystallographic structures have been shown to support superconductivity. As shown in Fig. 1.1a, they include LiFeAs [9] (111 family),

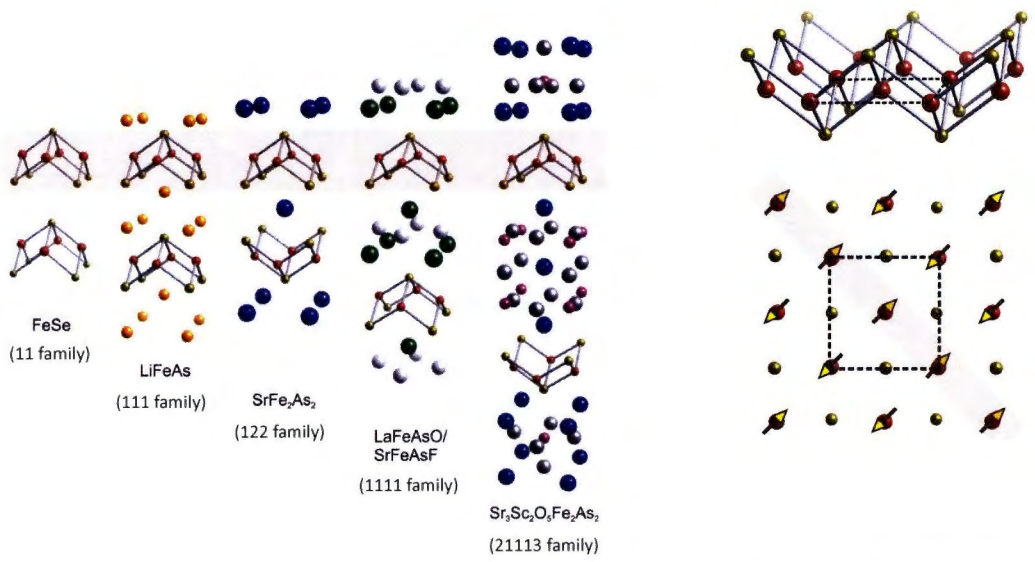

(a) Crystal structure (b) magnetic structure

Figure 1.1: Crystal structures of several families of the iron-based superconductors and magnetic structure of the iron-based superconductors. From [13]

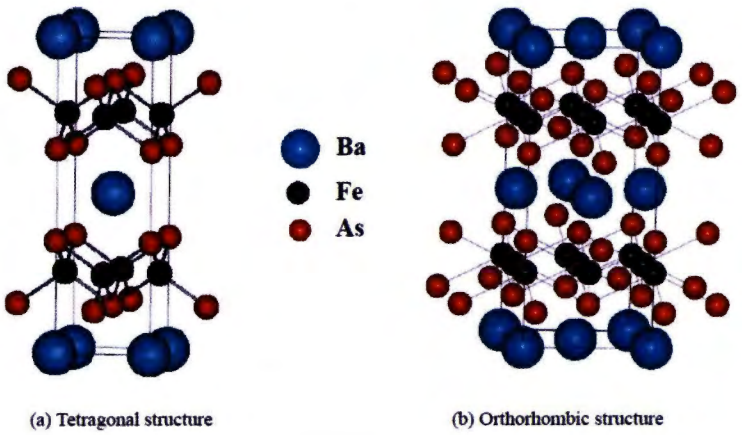

Figure 1.2: Crystal structure of $Ba(Fe_{1x}Co_x)_2As_2$

$Fe_{1+y}Te_{1-x}Se_x$ [10] (11 family), $(Fe_2P_2)(Sr_4Sc_2O_6)$ [11] (21113 family), and $Ba_{1-x}K_xFe_2As_2$ [12] (122 family), these structures all possess tetragonal symmetry at room temperature. A common structural feature for the iron-based materials is that it has a tetrahedral structure formed either by chalcogen elements (Se, Te) or pnictogen (P, As), and that iron atoms are located in the center of the tetrahedron. In this review we have

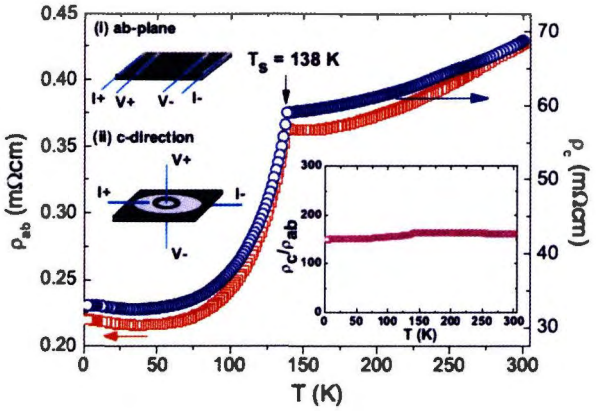

Figure 1.3: Electrical resistivity

studied about the iron-based 122 type $Ba(Fe_{1-x}Co_x)_2As_2$ compounds. The undoped parent compound of this family has a tetragonal crystal structure at high temperature. When the temperature decreases below the structural phase transition temperature T_S, a lattice distortion occurs and reduces the crystal symmetry from tetragonal to orthorhombic. The crystal structures of tetragonal and orthorhombic for $Ba(Fe_{1-x}Co_x)_2As_2$ are shown in Fig. 1.2. The lattice parameters $a = b$ =3.9625(1) $\AA$ and c =13.0168(3) $\AA$ for $BaFe_2As_2$. In the orthorhombic phase, the Fe-Fe lattice constant is elongated along one direction, and shortened along the other, as a result a stripe-type magnetic order sets in on the distorted Fe lattice. If we further lower the temperature below the T_N, a stripe-type long-range magnetic order sets in on the distorted Fe lattice. This stripe-type magnetic order also common for all of the FeAs-based superconducting systems. As illustrated in Fig. 1.1b, iron sub-lattice undergoes magnetic ordering with an arrangement consisting of ferromagnetically arranged spins along one chain of nearest neighbors within

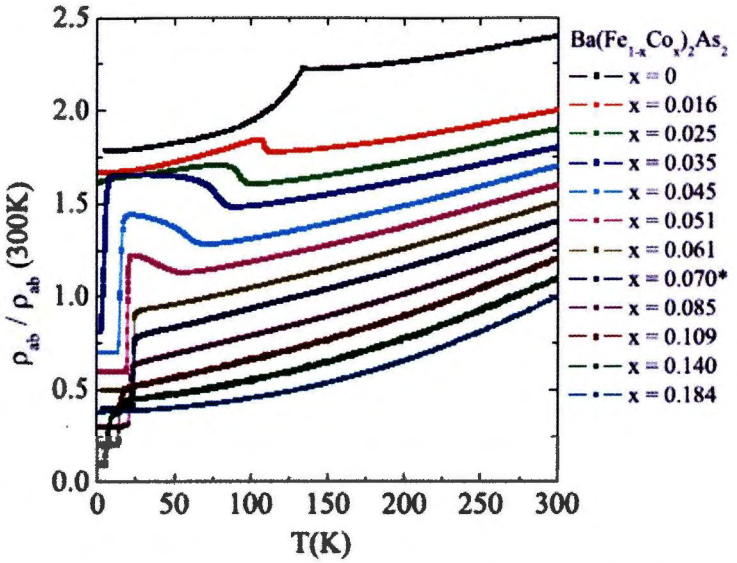

Figure 1.4: Electrical resistivity of $Ba(Fe_{1x}Co_x)_2As_2$ with various Co-concentrations. Figure from [4].

the iron lattice plane, and antiferromagnetically arranged along the other direction. This is displayed on a tetragonal lattice in the figure, but actually only occurs after these systems undergo an orthorhombic distortion. The parent compound $BaFe_2As_2$ has high electrical resistivity ρ at room temperature as illustrated for in Fig. 1.3, where the *ab*-plane resistivity at 300 K is 430 $u\Omega$-cm and the resistivity anisotropy ratio ρ_c/ρ_{ab} is about 150. The parent 122 compounds exhibit apparently coupled structural and commensurate antiferromagnetic (AF) transitions, also called spin density wave (SDW) transitions, at 140 K. As shown in Fig. 1.4 [4], with the substitution of Co with Fe ion the magnetic and superconducting transitions disappears and superconductivity comes out.

1.2 Phase diagram of $Ba(Fe_{1-x}Co_x)_2As_2$

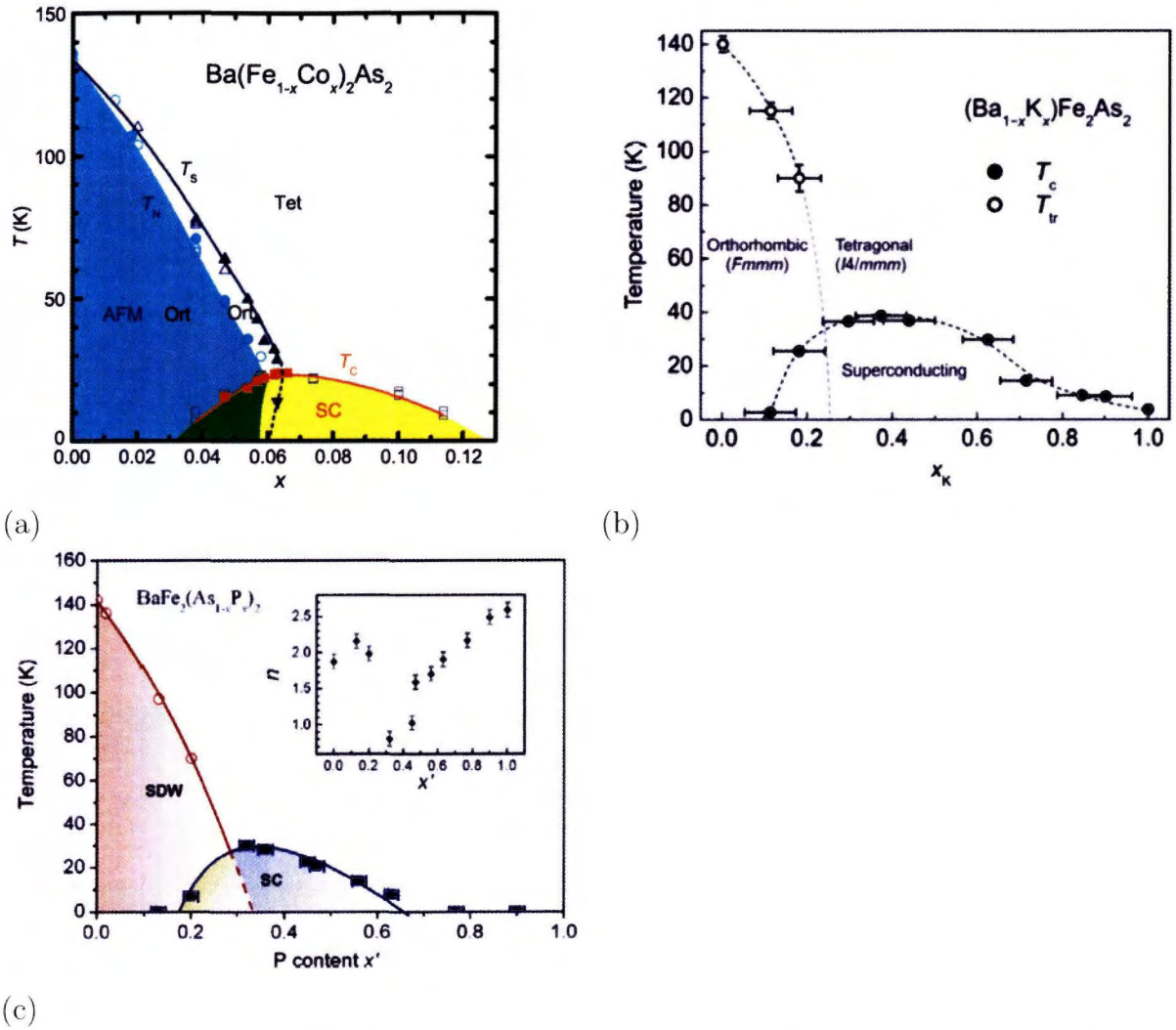

Figure 1.5: Schematic phase diagram of carrier doped and isovalent doped $BaFe_2As_2$. As representative materials, (a) electron-doped $BaFe_{1-x}Co_x)_2As_2$, (b) hole doped $(Ba_{1-x}K_x)Fe_2As_2$ and (c) isovalent doped $BaFe_2(As_{1-x}P_x)_2$ superconductors are shown.

The generic phase diagram of the iron-based systems can be deduced from either chemical doping/substitution or applied external pressure causes a change from an antiferromagnetic (AFM), parent compound to a superconducting (SC) state. A compilation of experimental phase diagrams is presented in Fig. 1.5 for the Ba-based Ba122

systems, for electron-doped $Ba(Fe_{1x}Co_x)_2As_2$ in Fig 1.5(a), hole-doped $(Ba_{1x}K_x)Fe_2As_2$in Fig 1.5(b), and isovalent doped $BaFe_2(As_{1x}P_x)_2$ in Fig 1.5(c). These are the most widely studied of the five families and widely thought to capture the main traits of all FeSCs. In small doping region, these compounds show AFM (spin density wave: SDW) phase, and with increasing doping level, the SC phase appears. Interestingly, in the underdoped and optimally doped compounds, the SC, structural and AFM phases coexist and show the highest T_{sc} for each compounds. For example, in the case of hole-doped K-Ba122, the SDW order and superconductivity coexist at low temperature for $0.2 < x < 0.4$. Another point in the phase diagram is, the SC phase disappears around $x \sim 0.15$ for $Ba(Fe_{1-x}Co_x)_2As_2$, while the SC phase of $Ba_{1x}K_xFe_2As_2$ still remains in the heavily overdoped region.

In the phase diagram of $Ba(Fe_{1-x}Co_x)_2As_2$, we can see that a coexistent phase of superconductivity and the magnetic order. It is also clear that T_{sc} takes the highest value just when both the structural phase transition and the magnetic order are suppressed. Such behavior, appearance of superconductivity along with the disappearance of the adjacent order, has been recently observed in many systems such as UCoGe and $CePd_2Si_2$, where superconductivity appears near the quantum critical point (QCP) [17, 18].

1.3 Tuning of phase diagram in pnictides

As in the cuprates, chemical substitution also plays a key role in inducing the superconducting phase as in iron-pnictides. It has been argued that there are some similarities between the recently discovered Fe-based superconductors and high T_{sc} cuprates or heavy Fermion superconductors. The most important similarity is that all of them are close to the magnetically ordered state, which suggests the contribution of magnetic fluctuation to the superconductivity pairing mechanism. The electronic phase diagrams of T_{sc} versus x show a dome-shaped curve in all cases. The parent compound of cuprate superconductors is a Mott insulator and the number of doped holes/electrons is a key parameter that controls the occurrence of superconductivity via the weakening of the electron correlation. In the case of a heavy Fermion compound, pressure is an important parameter that controls the product of the exchange interaction and the density of states in the Doniach phase diagram [19]. In iron based superconductors the tuning parameter of the phase diagram is still under debate. The effect factor to T_{sc} in iron based superconductors studied by various ways. As we know the parent compound of iron-based superconductors is a metal, exhibiting a spin density wave at low temperatures. Superconductivity is induced either by chemical substitution or the application of pressure, so the phase diagram of iron based superconductors have been studied by doping effect and pressure effect.

As shown in Fig. 1.5, the quantitative similarity between phase diagrams produced by substitutions involving both obvious (*i.e.*, K^{1+} for Ba^{2+}) [20] and subtle (*i.e.*, Co-$3d^7$ for Fe-$3d^6$) [21] charge doping, as well as nominally isovalent (P-$3p^3$ for As-$4p^3$) [22] substitutions, is enticing due to the implied versatility of chemical tuning parameters available to experimentalists for studying these systems. Furthermore, it promotes the idea that simple charge doping, as understood to be the case in the cuprates, is not the sole factor in determining the phase boundaries of these systems and that structural tuning may play a role.

Pressure tuning is less well understood. In some cases this powerful control parameter is aligned with its chemical substitution counterpart. For instance, in $Ba_{1-x}K_xFe_2As_2$ a good overlap exists between lattice parameter variation by applied pressure or K substitution [23], allowing conclusions about the roles of lattice structure versus charge doping to be made. There is still a question that whether doping induces the phase diagram or pressure induces the phase diagram. Recently S. Drotziger et al.[19] studied about this problem by tuning both hydrostatic pressure and Co concentration (x) on T_{sc} and various structural parameters such as Fe-Fe distance d_{Fe-Fe}, bond angles ϕ_i, Fe_2As_2 layer thickness (pnictogen height) h_{Fe-As}, c/a ratio, and bond length d_{Fe-As} in detail. They found that all the data points of T_{sc} lay on a single curve, as shown in Fig 1.6, if they assumed that 1% Co doping corresponds to the application of a pressure of 1.275 GPa. This demonstrates that Co concentration

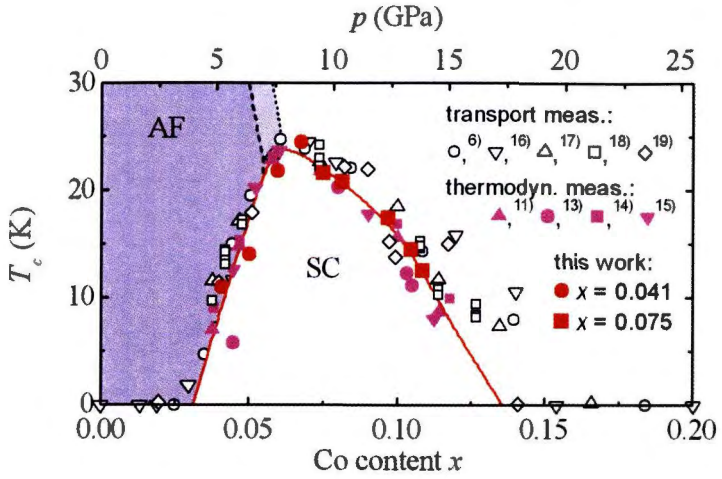

Figure 1.6: Phase diagram of $Ba(Fe_{1-x}Co_x)_2As_2$ as a function of x (lower axis). The open symbols and the pink-colored symbols denote data of other groups[24], and they are determined by resistivity and thermodynamic properties, respectively, at p = 0. The solid red symbols represent the authors' data, and they are plotted as a function of p (upper axis) by assuming $\Delta p/\Delta x = 0.125$ GPa/at.%-Co. Figure from the [19].

and pressure have an identical effect on the electronic state. In other words, electron doping by Co substitution is less important than the effect of lattice contraction due to Co substitution. In order to find a key parameter, the authors compared the $x-$ and p-dependence of various structural parameters. They examined the most promising parameters such as the c/a ratio, Fe-Fe distance, As height from the Fe layer, and As-Fe-As bond angle. All these parameters change linearly with x and p, but the slopes for x and p differ significantly. In some cases, the slope is positive for x, while it is negative for p. The only parameter whose $x-$ and p-dependence are similar to each other is the Fe-As bond distance, as shown in Fig 1.7. Since the p-dependence of this parameter is very weak, a more detailed structure analysis may be necessary.

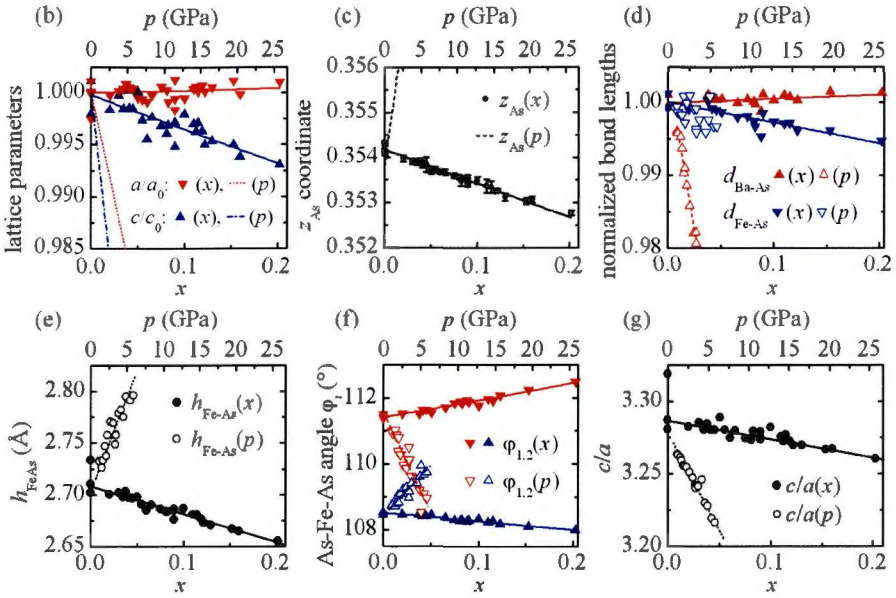

Figure 1.7: Normalized various structural parameters as functions of x and p. Figures are taken from the [19].

1.4 Previous work about the elastic properties of Iron based superconductors

A discussion follows on the various experimental techniques used for ultrasonic investigations. In our research we have used ultrasonic pulse echo method. In a elastic constant measurement, elastic constant C can be obtained by the sound velocity v of the longitudinal and transverse wave by the formula of $C = \rho v^2$, where ρ is the sample density. In ultrasonic measurement the ultrasound travels in a solid and deforms the crystals locally, lowering the symmetry of the sample. The strains introduced in to the solid were classified into irreducible representations of the point group. Fig. 1.8 shows the temperature dependence of all elastic constants for $Ba(Fe_{0.963}Co_{0.037})_2As_2$. Usually, elastic constants show gradual increases as T decreases, which is typical behavior for any

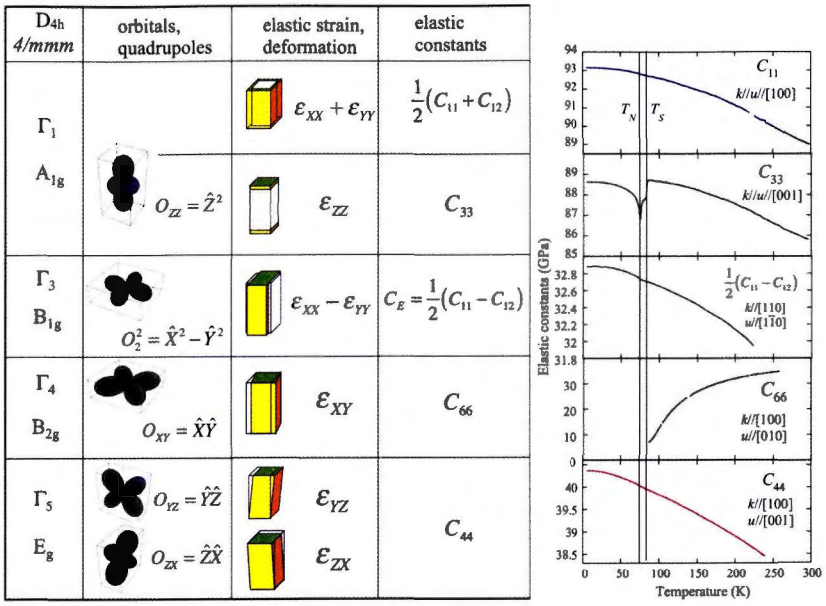

Figure 1.8: Orbitals, quadrupoles, elastic strains and their corresponding elastic constants classified into the irreducible representation of point group D_{4h}. Temperature dependence of all elastic constants of $Ba(Fe_{0.963}Co_{0.037})_2As_2$ are shown in the figure.

material, reflecting phonon anharmonicity. Among all elastic constants in Fig. 1.8, large elastic softening has been observed in C_{66}, which extends to 90% from room temperature toward low temperatures. No large anomaly was found in the other elastic constants. In elastic constant measurements, the local symmetry of the crystal is collapsed by the introduced sound waves. There are two types of couplings between the order parameter Q and the elastic strain ε. Namely, a bilinear coupling having the form of $Q\varepsilon$ and a magneto-strictive (magneto-elastic) coupling with the form of $Q^2\varepsilon$. Because both couplings cause the lowering of the crystal symmetry, the elastic strain has been called as Symmetry Breaking Field. However, the magnetostrictive coupling brings about no large elastic anomaly in general as compared to a bilinear coupling. So

it is obvious that the observed large anomaly in C_{66} is ascribed to the bilinear coupling. In the case of $Ba(Fe_{1-x}Co_x)_2As_2$, as shown in Fig. 1.8 the ε_{xy} strain as a perturbation field of C_{66}, which belongs to the B_{2g} representation of D_{4h}. It deforms the crystal symmetry from tetragonal to orthorhombic. In the case of $\varepsilon_{xx} - \varepsilon_{yy}$ for $\frac{1}{2}(C_{11} - C_{12})$ and $\varepsilon_{yz}(\varepsilon_{zx})$ for C_{44} the deformed symmetry is orthorhombic and monoclinic, and they belong to B_{1g} and E_g, respectively. The interesting physical quantities such as the charge, orbital (d-electron systems), or electric quadrupole (f-electron systems) belong to the reproducible representations, and are equivalent to those of the elastic strains. The orbitals (quadrupoles) belonging to each irreducible representation are shown in Fig. 1.8. We can obtain the information on these quantities through the coupling with the elastic strains as elastic softening.

The first elastic measurement for the iron-based superconductors was performed by McGuire et al. for polycrystalline sample LaFeAsO (1111 family) [25]. They used Resonant Ultrasonic Spectroscopy method for the measurements. As shown in Fig. 1.9, they studied the elastic constants C_{11} and C_{44} of this sample and reported remarkable softening towards low temperatures and discovered a elastic anomaly at structural phase transition, but the anomaly at structural phase transition still not clear. Subsequently, Fernandes et al. have studied the elastic property of $BaFe_2As_2$ and Co-doped Ba122 system $Ba(Fe_{1.84}Co_{0.16})_2As_2$ [26]. They have also used Resonant Ultrasonic Spectroscopy method for the experiment. As shown in Fig. 1.11 both materials show a large

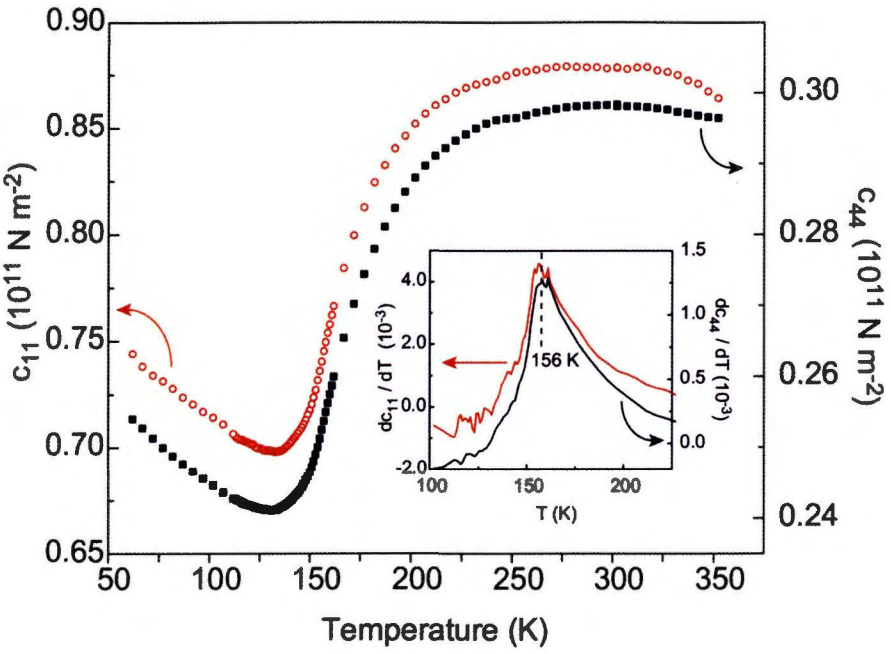

Figure 1.9: (Color online) Elastic constant C_{11} and C_{44} of $LaFeAsO_{1-x}F_x$. From Ref. [25]

elastic softening in C_{66} towards low temperatures. They explained the origin of the elastic anomaly in C_{66} by spin-nematic order. In iron-based superconductors two iron atoms are present in one tetragonal unit cell, as shown in Fig. 1.10 (open blue circles and filled red circles), which form two AFM sub-lattices with coplanar staggered magnetic moments m_1 and m_2. If the two spins with the antiparallel configuration couple with each other, which fluctuates correctively, this coupled spins called spin-nematic order parameter can couple linearly with the elastic strains. In a elastic constant measurement, there are only two types of coupling between the order parameter and the elastic strain. Namely bilinear coupling and magneto-elastic coupling. Magneto-elastic coupling does not cause a large elastic anomaly in general as compared to a bilinear

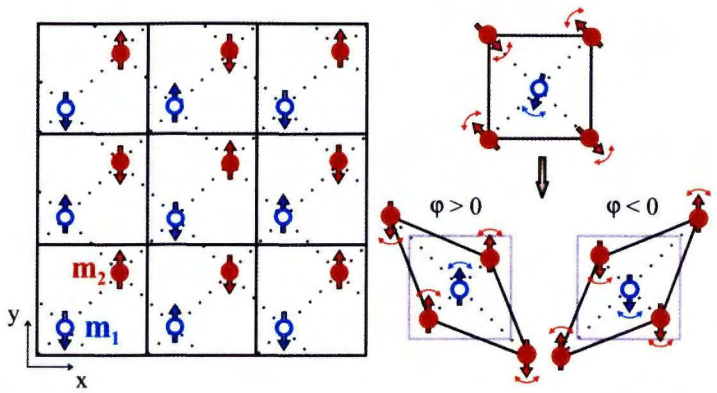

Figure 1.10: (Color online) Schematic illustration for the mechanism of nematic spin configuration. From Ref. [26]

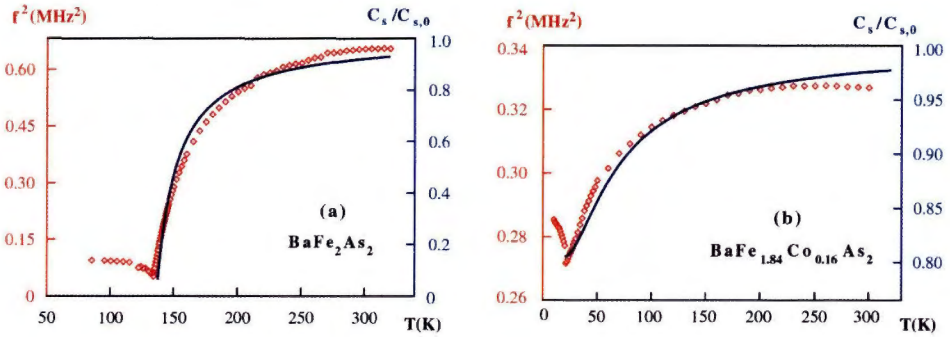

Figure 1.11: (Color online) Temperature dependence of elastic constant C_{66} for both (a) undoped $BaFe_2As_2$ and (b) optimally doped $Ba(Fe_{1.84}Co_{0.16})_2As_2$. From Ref. [26]

coupling. In Fernandes et al. research the spin-nematic order can couple with the elastic strain with a bilinear form.

But bilinear coupling on the basis of the Jahn-Teller expression is prohibited between spins and strains, since time-reversal symmetry is broken in the spin system. The anomalous C_{11} and C_{44}, which were reported by McGuire et al. are not confirmed, because the elastic anomaly is expected in C_{66} for the 1111 system from the viewpoint of the structural change of this system. The latter one, which is the elastic anomaly in C_{66} for Ba122 measured by Resonant Ultrasonic Spectroscopy method

for the measurement, in this method it is difficult to assign the mode of elasticity. But we know from this research that a large elastic anomaly occurs in C_{66} for Ba122. Anyway, these studies of the elastic property for iron based superconductors give us a great interest.

We measured the temperature dependence of elastic constants of C_{11}, C_{33}, C_{44}, $\frac{1}{2}(C_{11} - C_{12})$ and C_{66} for bulk single crystals of eight different Co concentration samples of $Ba(Fe_{1-x}Co_x)_2As_2$, in which Co concentration ranges from $x = 0$ to 0.245. Single crystals were grown by a flux method, and Co concentration was determined by energy dispersive X-ray spectrometry (EDS) analysis. In our study it shows very large elastic softening in C_{66}, the amount of softening is 90% for un-doped sample and it reaches 80% for $Ba(Fe_{0.963}Co_{0.037})_2As_2$. For the overdoped samples, the anomalies in C_{66} gradually disappear with the increasing of Co concentration. By calculating the elastic compliance S_{66}, we have found a clear correlations between superconducting transition temperature and the amount of anomaly in S_{66}, and results highlight that the importance of structural fluctuations for the emergence of superconductivity. Elastic constants of bulk single crystals of Co-doped $BaFe_2As_2$ were measured by Goto et al [28]. They reported the temperature dependence of C_{11}, C_{33}, C_{44}, $\frac{1}{2}(C_{11} - C_{12})$ and C_{66} and found a particularly large elastic softening in only C_{66} for the single crystalline $Ba(Fe_{0.9}Co_{0.1})_2As_2$ grown by a Bridgman method. Results are shown in Fig. 1.12.

As shown in Fig. 1.8, $Ba(Fe_{0.963}Co_{0.037})_2As_2$ shows two small but remarkable elastic anomaly in C_{33}, which are corresponds with the struc-

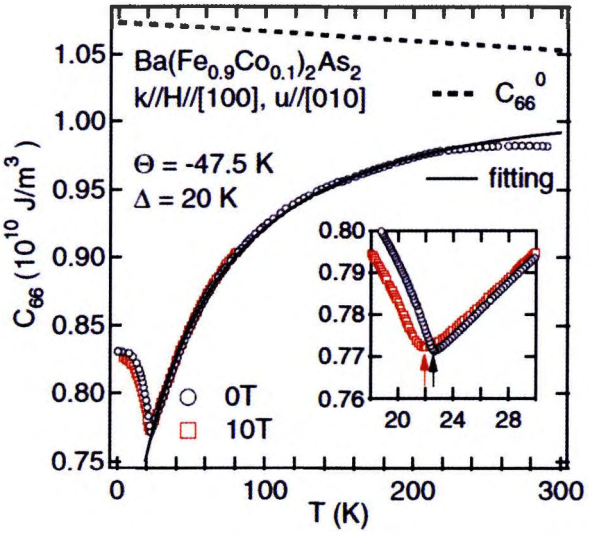

Figure 1.12: Temperature dependence of elastic constant C_{66} of $Ba(Fe_{0.9}Co_{0.1})_2As_2$. Figure printed from the Ref. [28].

tural and magnetic transitions of this sample. Occurring an elastic anomaly in C_{33} is quite peculiar, because c-axis property would be considered to be irrelevant for the layered structure of this material. We think this anomaly in C_{33} is common for other components of Co doped iron-based superconductor $Ba(Fe_{1-x}Co_x)_2As_2$, and these anomalies originate from the magneto-strictive coupling. In this thesis we discuss the anomaly in C_{66} and C_{33}.

1.5 Purpose of this study

The discovery of superconductivity in $LaFeAsO_{1x}F_x$ in 2008 opened up a new field in superconductivity research. Now, many types of new iron-based superconductors have been fabricated. Iron based superconductors have high critical temperature T_{sc}, it is as high as cuprate su-

perconductors, so it has attracted many researchers for its promising applications. Now studies focus on the mechanism of superconductivity of this family, but the key parameter mediating the superconducting state is not clear yet. In this system superconductivity is induced either by chemical substitution or the application of pressure. On the mechanism of superconductivity, it has been argued about the role of structural and magnetic fluctuations as mediating parameters of superconductivity. Among all iron-based superconductors with different crystal structures, $Ba(Fe_{1-x}Co_x)_2As_2$ is suitable for basic research, because it can provide large single crystals. The parent compound $BaFe_2As_2$ of this system shows stripe magnetic order with a structural change from tetragonal to orthorhombic. If a system encounters with the structural phase transition, elastic constant is a suitable probe for investigating of the neighboring structural ordering. At first, we have reported elastic properties of iron-based superconductors $Ba(Fe_{1-x}Co_x)_2As_2$, and found the structural fluctuation in C_{66} associated with the structural (T_S) and magnetic phase transitions (T_N). Our results suggested the importance of orbital fluctuation in the emergence of superconductivity. Starting from our reports, many researchers have discussed the superconductivity based on the orbital fluctuations. On the other hand, the structural fluctuation leads to an in-plane order, and it possesses two-dimensional nature. However, an order is hard to occur in two-dimensional systems, so three-dimensionality is necessary for the occurrence of ordering. Next, in this thesis, we have focused our attention on the three-dimensional

character of this system. In our experimental tool, ultrasonic measurement, the corresponding elastic strain ε_{ZZ} modulates physical quantities along c-axis through the elongation and contraction of the inter-layer spacing. So by examining the corresponding elastic constant C_{33}, we can obtain the three-dimensional character of this system. Our results show that the elastic anomaly C_{33} due to the inter-layer fluctuation is enhanced near the QCP (Quantum Critical Point). We have studied it by means of electrical resistivity, heat capacity, ultrasonic attenuation in addition to elastic constant C_{33}. It is obvious from my results that the three-dimensional properties of Ba122 possibly originated from the magnetic character of this system. My findings about the correlation of C_{33} with T_{sc} as well as the in-plane fluctuation appearing in C_{66} would highlight the roles and relations of the orbital and magnetic fluctuations in the emergence of superconductivity.

Chapter 2

Experimental apparatuses and Experimental method

2.0.1 Ultrasonic measurement

2.0.2 Pulse echo method

In this research we have used the ultrasonic pulse echo method. It is used to measure the frequency area of $10 \sim 500$ MHz. Figure. 2.1 shows the outline of the ultrasonic measurement apparatus. High-frequency signal pulses are generated by a pair of piezoelectric transducers, which are bonded on the parallel planes of the sample. The transducer converted electric signal to ultrasonic one. The ultrasound generated at one side propagates to the other side, and is reflected at the surfaces repeatedly. In this experiment, we used Thiokol to adhesion the sample, and $LiNbO_3$ for the transducer. By examining pulse echo time interval and

the specimen length, we can obtain the sound velocity

$$\nu = \frac{2l}{\Delta T} \tag{2.1}$$

The elastic constant is obtained by using the formula

$$C = \rho\nu^2 \tag{2.2}$$

where ρ is the density of the sample. As the ultrasound travels through the sample, ultrasonic signal intensity is attenuated by absorption. By this attenuation, pulse echo intensity attenuates exponentially according to equation (1-3), and these attenuated pulse echo sequence is shown in Fig. 2.2.

$$I = I_0 exp(-\beta\Delta T) \tag{2.3}$$

Here, I is the echo intensity and ΔT the time interval. By measuring the ratio of the height of the adjacent ultrasonic pulse-echo, we can obtain the required absorption coefficient β at per unit time

$$\beta = \frac{20log(I_n/I_{n+1})}{\Delta T}[dB/cm] \tag{2.4}$$

In addition, because the interval time of echo ΔT corresponds to the distance $2l$, the absorption coefficient at per unit α

$$\alpha = \frac{20log(I_n/I_{n+1})}{2l}[dB/cm] \tag{2.5}$$

We can obtain the absolute value of absorption coefficient.

2.0.3 Phase caparison method

Phase comparison method is a way to replace the amount of change observed frequency variation of the speed of sound propagating through the sample, by calculating the speed of sound ν, elastic constant C can be determine. Figure. 2.3 describes the operating principle of ultrasonic measurement apparatus according to the phase comparison method. As seen in the scheme a signal transmitted from Synthesizer (MG2502), and this signal is separated into two directions and enters (Double Balanced Mixer) DBM as the reference signal V_{ref}, while the other is converted to a ultrasonic pulse-echo by the Diode Switch which is controlled by the Pulse Generator. This signal is convert into ultrasonic pulses by a transducer and propagates through the sample. After these ultrasonic pulses repeating reflections at both ends of the sample with a speed of v, converted again into an electric signal by transducer on the opposite side. While ultrasonic pulse passing through the sample, a delay is occur, and this delay is is proportional to the propagation time in the sample, so there is phase difference is occur between the ultrasonic pulse and reference signal. The reference signal is

$$\nu_{ref} = Acos(2\pi ft) \tag{2.6}$$

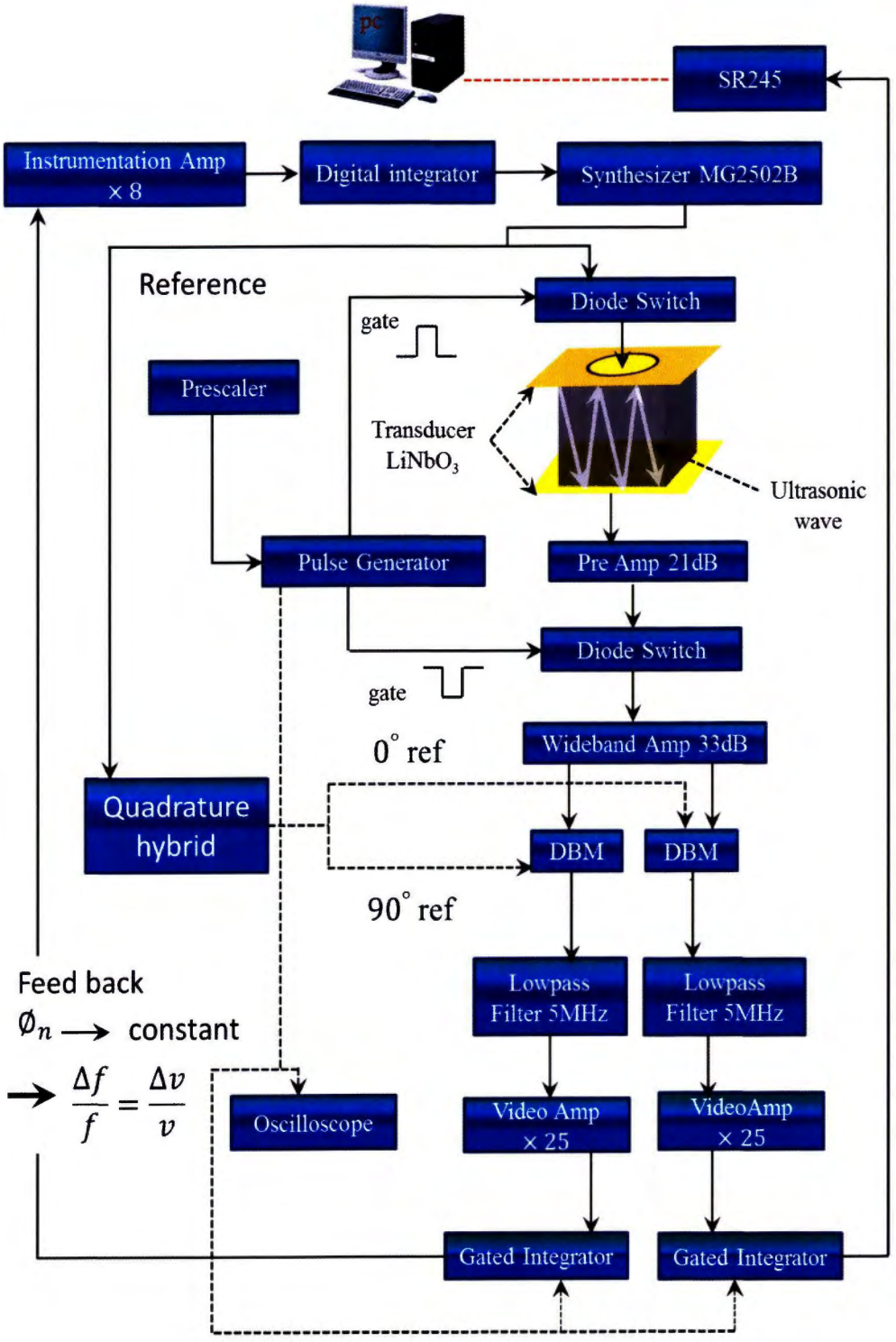

Figure 2.1: Outline of the ultrasonic measurement apparatus.

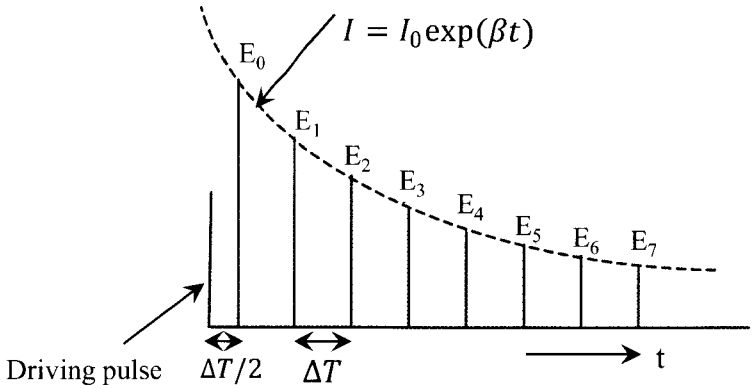

Figure 2.2: Pulse echo sequence.

The n^{th} pulse-echo ultrasound ν_{sn} is

$$\nu_{sn} = Bexp[-\alpha(2n+1)l]cos(2\pi ft + \phi_n) \tag{2.7}$$

where α is the ultrasound absorption coefficient per unit length, ϕ_n is the reference signal for the n^{th} echo pulse. The output signal from the mixer can be describe by the ν_{ref} and ν_{sn}

$$\nu_{out} = \nu_{ref} \times \nu_{sn} = \frac{1}{2}ABexp[-\alpha(2n+1)l]cos(2\pi ft + \phi_n) \tag{2.8}$$

where the first term is the alternating current component with a frequency of 2f, the second term is direct-current component that depends on ϕ_n. DC component which depends only on the phase difference by the cutting of AC component of the Low-Pass Filter:

$$\nu_{phase} = \frac{1}{2}ABexp[-\alpha(2n+1)l]cos\phi_n \tag{2.9}$$

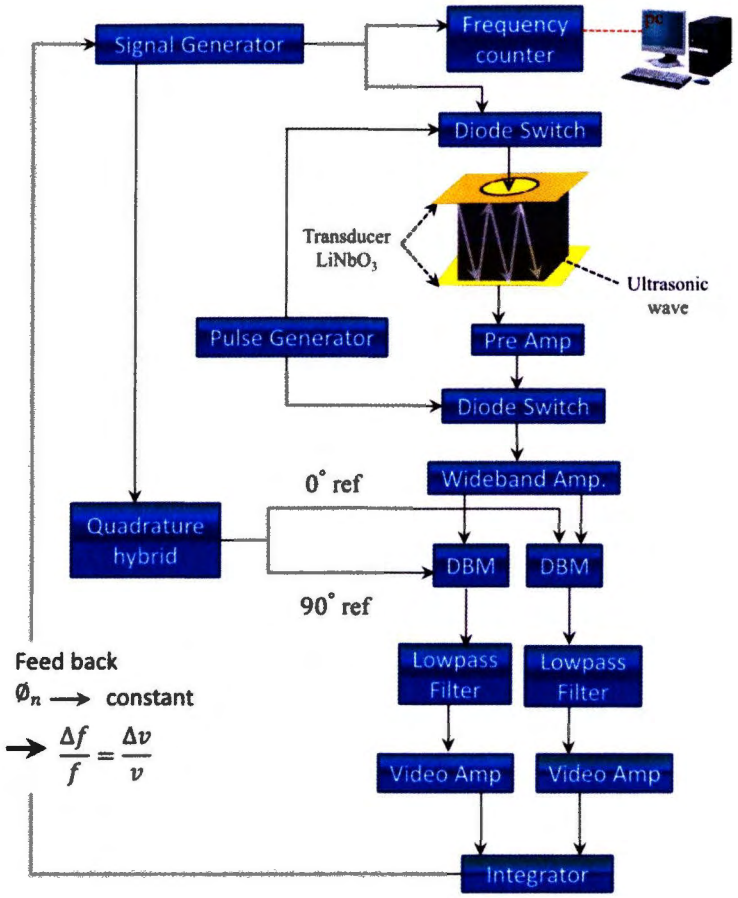

Figure 2.3: Outline of the phase comparison method.

where

$$\phi_n = 2\pi(2n-1)l\frac{f}{\nu} \tag{2.10}$$

Since the wavenumber of the Driving Pulse takes a constant value, then the changing of ν causes the changing of ϕ_n, that changes v_{phase}. To keep ϕ_n constant at $\pm 90°$, it needs to modulate only a frequency Δf which is feedback into Synthesizer. The changing of sample length is small enough to be ignored for the changing of velocity. So one can calculate the relative change of the sound velocity in a sample by the

relative change of frequency.

$$\frac{\Delta f}{f} = \frac{\Delta \nu}{\nu} + \frac{\Delta l}{l} \tag{2.11}$$

$$\frac{\Delta f}{f} = \frac{\Delta \nu}{\nu} \tag{2.12}$$

The absolute value of sound velocity can be obtained from the phase difference ϕ_n. If we replace the $f + \Delta f$ by f formula can be change:

$$\phi_n = 2\pi(2n+1)l\frac{f}{\nu} \tag{2.13}$$

changes to

$$\phi_n = 2\pi(2n+1)l\frac{f+\Delta f}{\nu} \tag{2.14}$$

Here, Δf is the frequency difference of 2π. Then we can establish a relationship between ν and f

$$\nu = (2n+1)l\Delta f \tag{2.15}$$

$$\nu = (2n+1)l\Delta f \tag{2.16}$$

2.1 Transducer

$LiNbO_3$ (lithium niobate) transducer was used to generate ultrasonic waves in the present study. $LiNb0_3$ transducers were synthesized by our group at Iwate prefecture researching center. The thickness of the

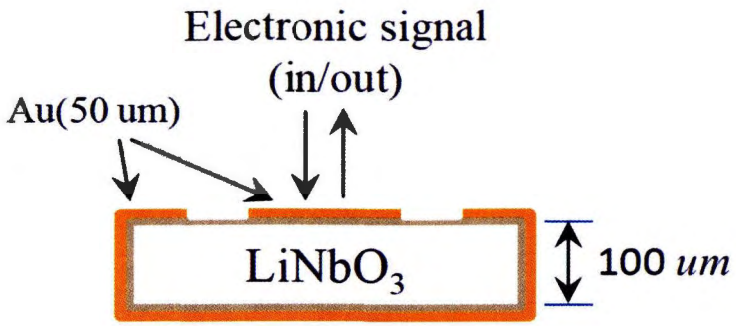

Figure 2.4: Transducer design.

$LiNbO_3$ plate is 100 *um*, 10 nm Ti and 100 nm Au sputtered on the substrate. In the case of $LiNbO_3$, the electromechanical coupling constant K is larger than that of quartz, it displays good dielectric constant and high longitudinal speed. $LiNbO_3$ is ideal for making high frequency transducers. The basic transducer designs for $LiNbO_3$ transducer is shown in Fig. 2.4. For oscillation of ultrasonic longitudinal and transverse wave, in this study we used a 41° transducer x-cut for transverse wave, and z-cut for longitudinal wave. These x-cut and z-cut transducers are shown in Fig. 2.5a and 2.5b. It is easy to a mistake for the confirmation of displacement direction of x-cut plate. The plate of the cutting machine does not rotate clockwise direction so it needs to rotate the plate to counterclockwise direction by 139°. The red line is the cutting direction and black line is the sub direction if Fig. 2.5a. In case of z-cut plate, it does not to confirm the displacement direction, so one can cut the plate according to the sub of line. The operating fundamental frequency for transverse wave is 17 MHz, and 33 MHz for longitudinal wave and both change to one of its odd harmonics.

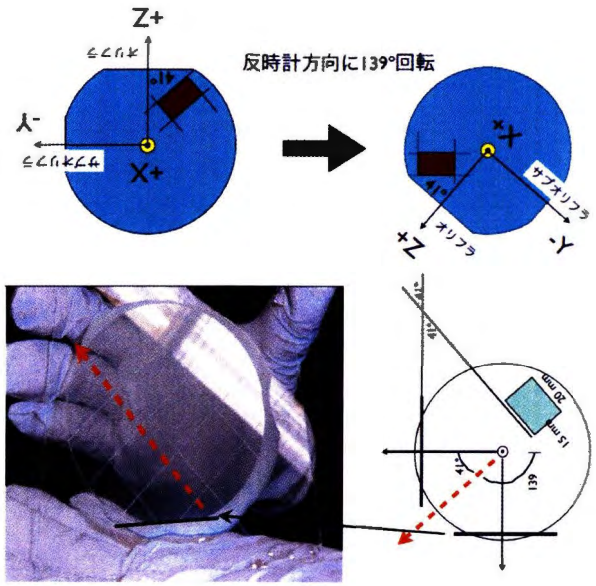

(a) x-cut transducer

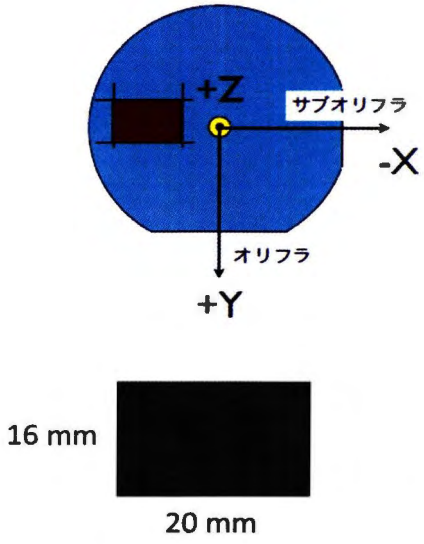

(b) z-cut transducer

Figure 2.5: (a) 41° transducer x-cut for transverse wave , (b) z-cut for longitudinal wave

2.2 Single crystal samples of $Ba(Fe_{1-x}Co_x)_2As_2$

The high-quality large single crystals of $Ba(Fe_{1-x}Co_x)_2As_2$ used in this work were grown by the self-flux method. Samples with eight Co concentrations $x = 0$, 0.037, 0.060, 0.084, 0.098, 0.116, 0.161, and 0.245 were prepared. The Co concentration in the grown crystals was determined by energy-dispersive X-ray spectroscopy (EDS). The Co content of the samples was about 75% of the prepared one. The samples were cut into a rectangular shape, after determining their axis by X-ray Laue photography. The sample had a typical area of $3 \times 3mm^2$ in the tetragonal ab (XY) cleavage plane, and a thickness of 2mm on the c-axis. The located positions on the phase diagram of these single crystal samples for elastic constant measurements of $Ba(Fe_{1-x}Co_x)_2As_2$ are shown in Fig. 2.6.

2.3 Electrical resistivity

We measured the electrical resistance simultaneously with the elastic constant for $x = 0.06$. This measurement was taken by using a conventional four-probe method, capton tape was interpolated between sample and transducer to avoid from short connection sample and transducer. Measurement circuit shown in Fig. **??**. This circuit was designed to measure resistance and elastic constant at one setting. In this way we can observe that where the elastic anomaly occurs superconducting phase transition or magnetic/structural phase transition for this sample, since

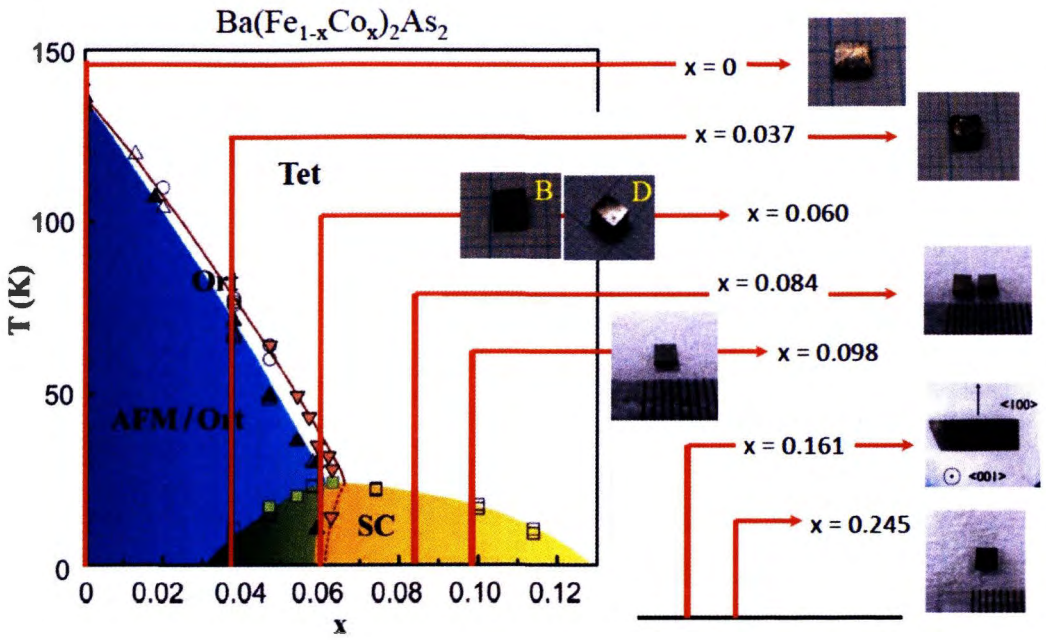

Figure 2.6: Single crystal samples and their position in the phase diagram.

the structural, magnetic and superconducting phase transition temperatures located closely to each other in $x = 0.06$. The resistivity ρ of a sample id defined as:

$$\rho = \frac{S}{L}R \tag{2.17}$$

where ρ is the resistivity, R is the resistance, S is the cross-sectional area of the sample, and L is the sample length.

2.4 Heat capacity

2.4.1 Experimental apparatus

Heat capacity was measured by PPMS, and this system has several special features for the heat capacity option.

Calorimeter Puck

The calorimeter puck (see Figure 2.7) contains a resistive platform heater, platform thermometer, and puck thermometer. The platform heater and platform thermometer are attached to the bottom of the calorimeter chip that functions as the sample platform. The puck thermometer is buried within the puck. The platform thermometer measures the temperature of the sample platform and thus the temperature of the sample. The puck thermometer measures the temperature of the puck, which serves as the calorimeter's thermal bath. Eight delicate, thermally conducting wires suspend the sample platform in the middle of the puck frame. These wires-four on each side of the platform-form the electrical connection to the platform heater and platform thermometer and also serve as the thermal connection between the platform and the puck frame. The puck frame and the wire guard help protect the wires, although the wires remain

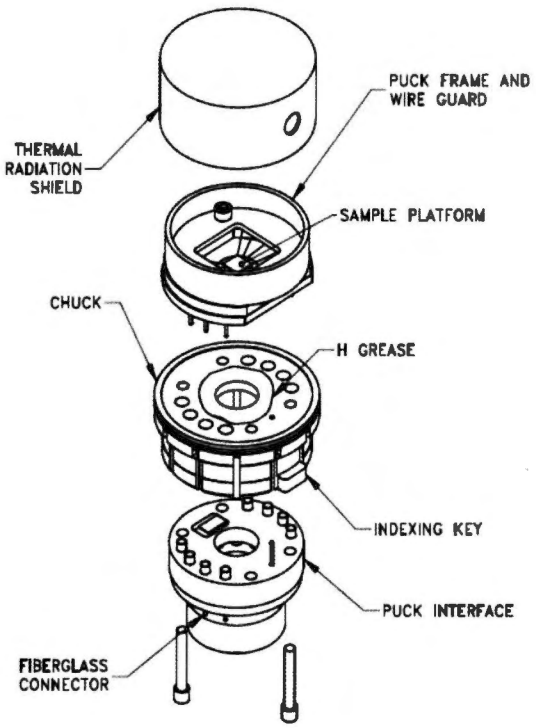

Figure 2.7: Exploded view of calorimeter puck

partially exposed. The chuck, which is below the puck frame and above the green fiberglass connector, produces the thermal contact to the base of the sample chamber. The chuck includes the indexing key, which drops into the indexing notch to lock the puck in position inside the PPMS sample chamber. The chuck, which is below the puck frame and above the green fiberglass connector, produces the thermal contact to the base of the sample chamber. The chuck includes the indexing key, which drops into the indexing notch to lock the puck in position inside the PPMS sample chamber.

Sample-Mounting Station

To prevent damage to the eight wires that hold the sample platform, the sample-mounting station uses a puck interlock arm and vacuum suction to stabilize the puck and platform. By stabilizing the puck and platform, the mounting station allows a sample to be easily mounted on the platform and removed from the platform while preventing the wires from being stressed. The puck interlock arm is curved to fit the circular exterior of the puck holder. When the interlock arm is pushed toward the holder, the interlock arm clasps and helps immobilize the puck. The vacuum supplied at the hose barb appears at the hole in the platform holder and sucks the platform downward to hold it in place. Small fingers on top of the platform holder further stabilize the platform.
The puck interlock arm is curved to fit the circular exterior of the puck holder. When the interlock arm is pushed toward the holder, the inter-

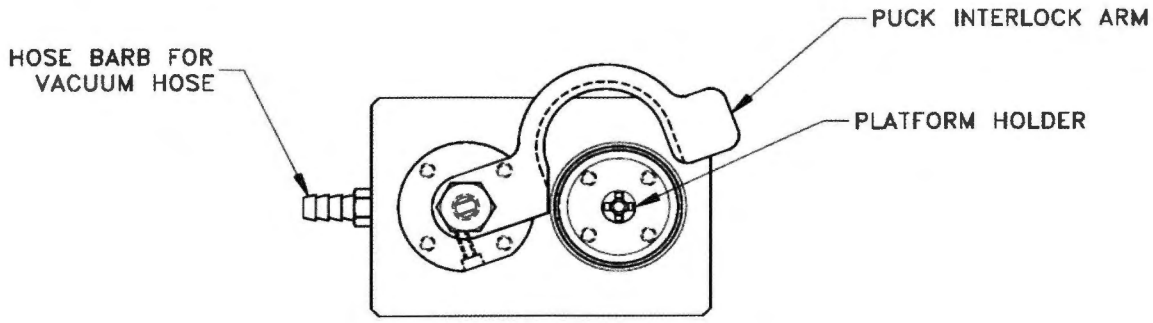

Figure 2.8: Top View of Sample-Mounting Station

lock arm clasps and helps immobilize the puck. The vacuum supplied at the hose barb appears at the hole in the platform holder and sucks the platform downward to hold it in place. Small fingers on top of the platform holder further stabilize the platform. The sample-mounting station is seen in Fig. 2.8.

The vacuum pump as seen in Fig. 2.9, is part of the sample-mounting station assembly. Vacuum is applied through the vacuum hose that attaches to the hose barb at the rear of the sample-mounting station.

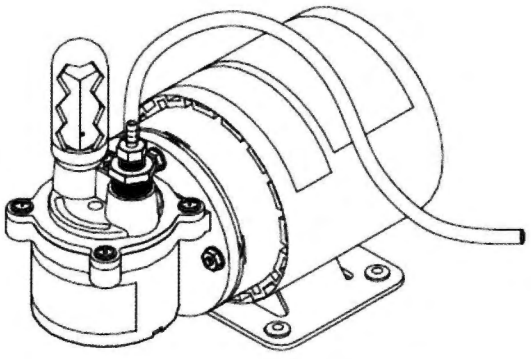

Figure 2.9: Vacuum Pump for Sample-Mounting Station

Chapter 3

Results

Elastic properties of iron based superconductor $Ba(Fe_{1-x}Co_x)_2As_2$ with various Co-concentrations were reviewed by ultrasonic measurement. Among them C_{66} shows large elastic softening towards to low temperatures, the amount of softening extends to 95%. There are two small softening were occurred in C_{33}, implies the three dimensional character of this system. C_{33} shows exotic softening near the QCP. We have studied it by means of specific heat, resistivity and ultrasonic attenuation in addition to the elastic constant.

3.1 Electrical resistivity of nearly optimal doped sample

$Ba(Fe_{0.94}Co_{0.06})_2As_2$ is located near to the QCP. For this Co concentration, we have studied the elastic properties, specific heat and electrical resistivity for two samples of different batch. The results of electrical resistivity was pictured in Fig. 3.1.

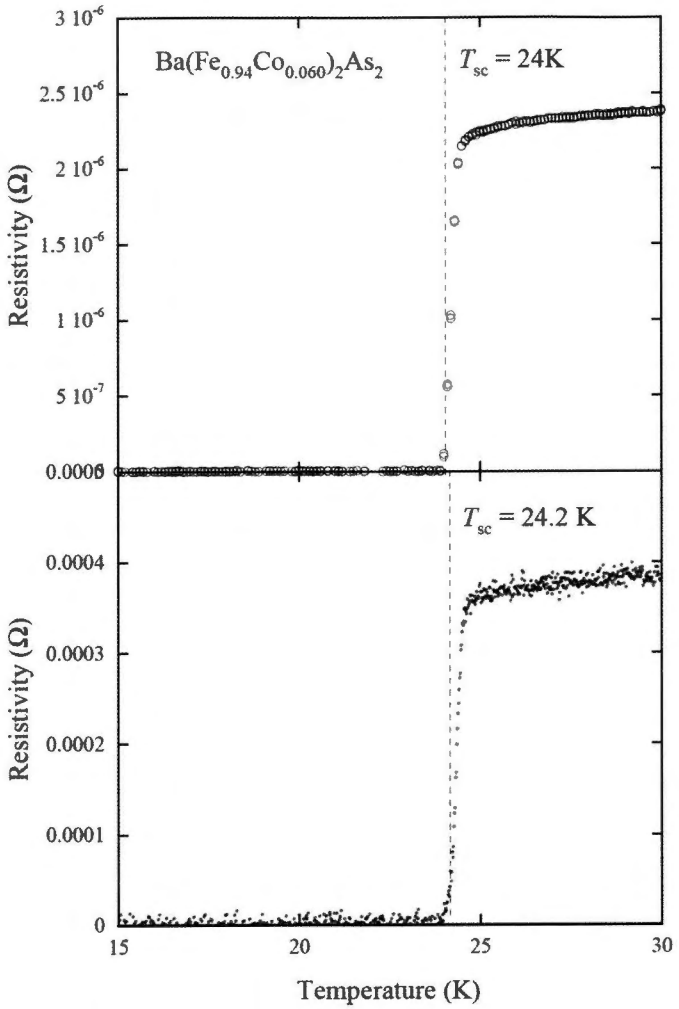

Figure 3.1: Temperature dependence of electrical resistivity of $Ba(Fe_{0.94}Co_{0.060})_2As_2$ for two different samples.

3.2 Results of heat capacity of $Ba(Fe_{1-x}Co_x)_2As_2$

We have also studied the heat capacity of $Ba(Fe_{1-x}Co_x)_2As_2$, where x=0, 0.037, 0.060, 0.084, 0.098, 0.161, 0.245 respectively. The results are shown in 3.2 for representative Co concentrations. We did not measure the heat capacity of 11.6% sample, because the sample weight exceeded the measurement range of the sample puck of PPMS. For undoped

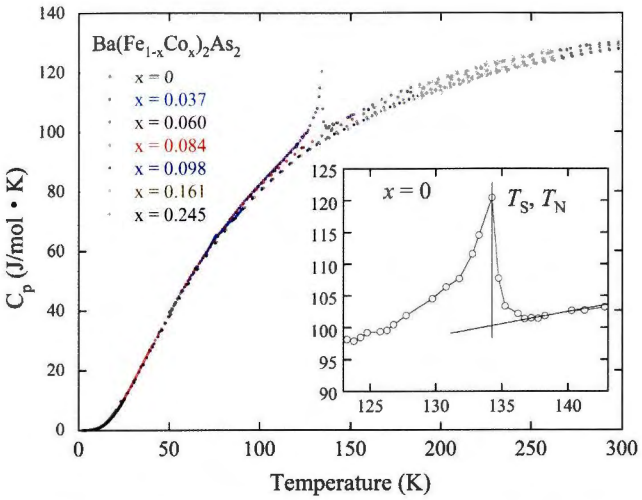

Figure 3.2: Temperature dependence of heat capacity of $Ba(Fe_{0.94}Co_{0.060})_2As_2$. In set shows the heat capacity near the phase transition of undoped sample.

$BaFe_2As_2$, a clear sharp peak occurs at structural/magnetic phase transition as shown in set of Fig 3.2, and this result comparable in value to other studies[43, 44]. Figure 3.3 shows heat capacity data near the transition temperatures for $x = 0.037$, 0.060, 0.084 and 0.098. Our data shows a clear specific jumps at phase transition temperatures.

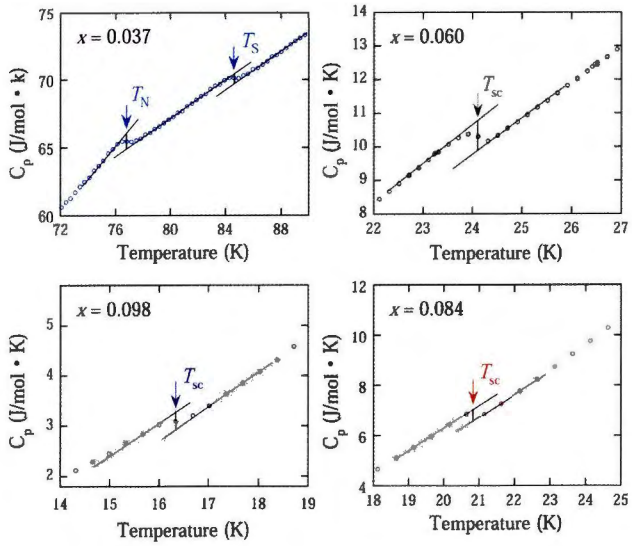

Figure 3.3: Heat capacity jump at the phase transition temperatures for $x = 0.037$, 0.060, 0.084, and 0.098 respectively .

3.3 Elastic constants for $Ba(Fe_{1-x}Co_x)_2As_2$

We have measured elastic constants for eight different Co concentrations of $Ba(Fe_{1-x}Co_x)_2As_2$ with 40 different modes. Elastic constants have been measured by an ultrasonic pulse-echo phase comparison method as a function of temperature from 5 K to 300 K by using a cryostat equipped on a Gifford-McMahon (GM) Cryocooler. Except for C_{66}, all elastic constants show monotonic increase with the decreasing of temperature. They show elastic anomalies at structural, magnetic and superconducting phase transition temperatures. We will introduce the results of elastic constants for these samples as follows.

3.3.1 Temperature dependence of elastic constants in $BaFe_2As_2$

In the case of undoped sample as shown in Fig. 3.4, all elastic constants show an elastic anomaly at 134 K, it corresponds to the structural and magnetic phase transition temperatures. The amount of softening for 0.7% for C_{11}, 4.3% for C_{33}, 90% for C_{66}, and C_{44} shows elastic hardening of 0.2%. C_{11} and C_{44} shows hysteresis at this transition temperature, implies that the first order phase transition temperature. Hysteresis are described in Fig. 3.5.

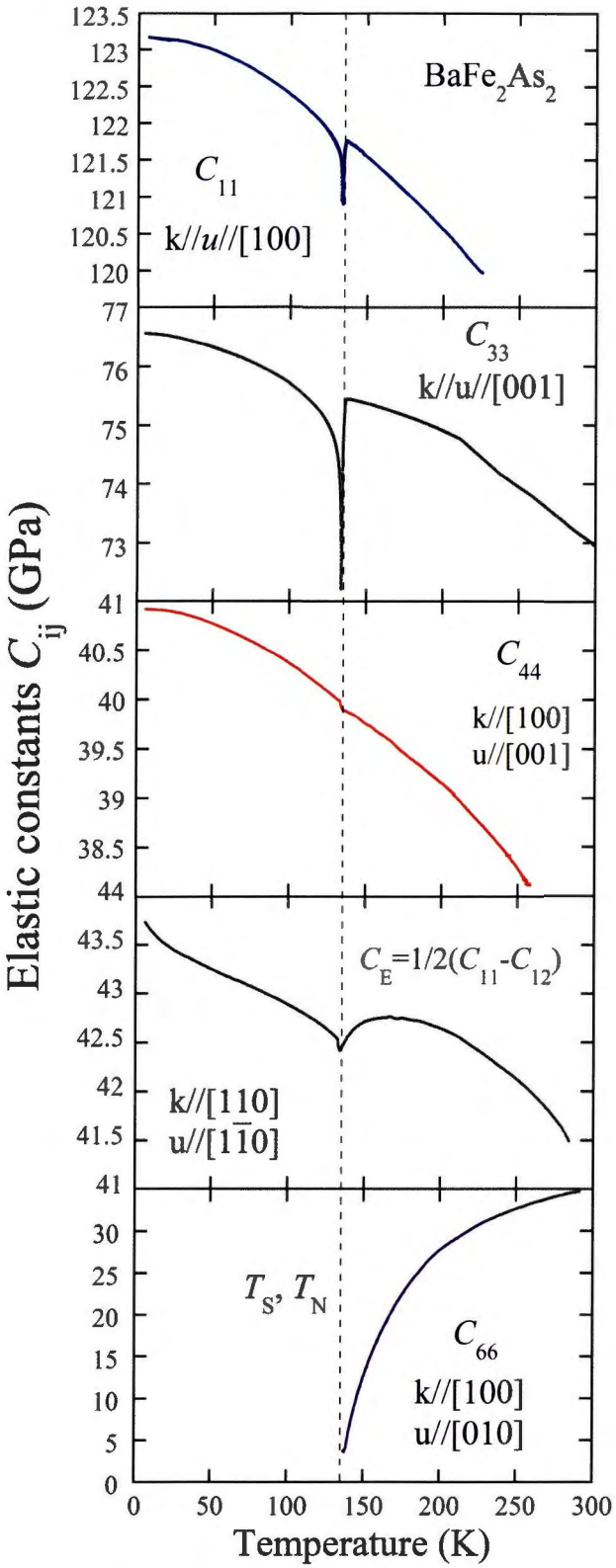

Figure 3.4: Temperature dependence of elastic constants C_{ij} of $BaFe_2As_2$. Where C_{ij} represents C_{11}, C_{33}, C_{44}, $\frac{1}{2}(C_{11} - C_{12})$, and C_{66}

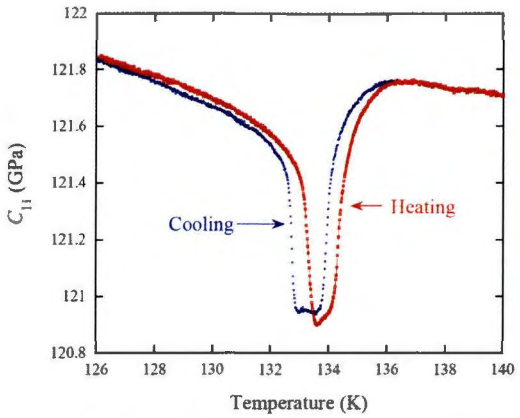

(a) Elastic constant C_{11} near the phase transition temperature.

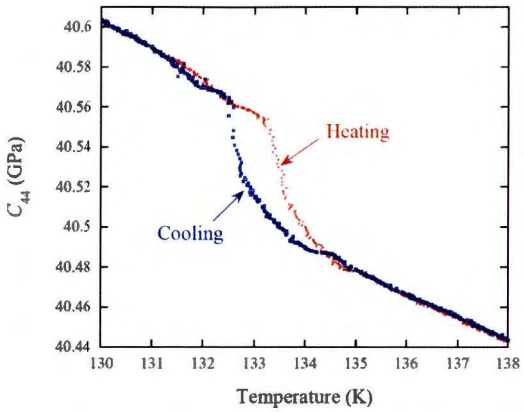

(b) Elastic constant C_{44} near the phase transition temperature.

Figure 3.5: Appearing an elastic hysteresis at the phase transition temperature in undoped iron based superconductor $BaFe_2As_2$.

3.3.2 Temperature dependence of the elastic constants C_{ij} of $Ba(Fe_{0.963}Co_{0.037})_2As_2$.

This composition located at the underdoped region in the phase diagram of $Ba(Fe_{1-x}Co_x)_2As_2$. It shows structural, magnetic and superconducting phase transitions at certain temperatures. Fig. 3.6 shows the temperature dependence of elastic constants C_{ij}. All elastic constants show an elastic anomalies at structural (T_S =84.7 K), and magnetic phase transition temperature (T_N =75 K). In the case of C_{66} it shows very large elastic softening, the amount of softening is reached to 80%. The echo signal was disappeared at T_S. So it is unavailable to measure the elastic constant below 84.7K for C_{66}. In the case of C_{33} it shows remarkable elastic softening at structural and magnetic phase transition temperatures. Unfortunately our experimental equipment does not decrease enough to the superconducting phase transition temperature

of this sample. The other elastic constants C_{11}, C_{44}, and $\frac{1}{2}(C_{11} - C_{12})$ show small elastic anomalies at structural and magnetic phase transition temperatures.

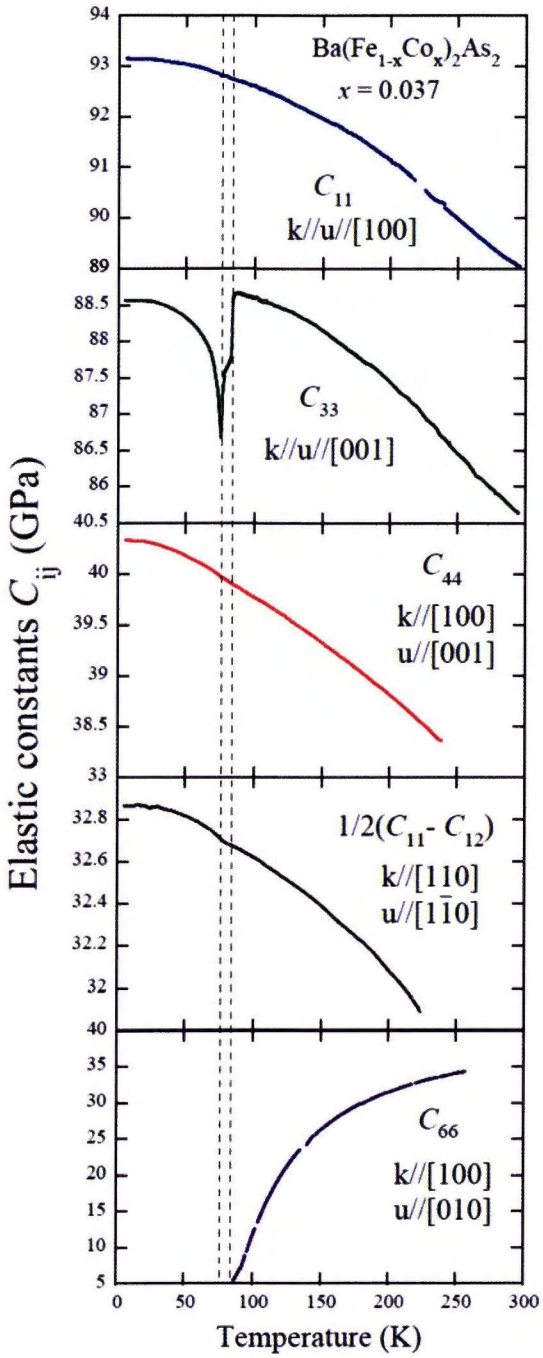

Figure 3.6: Temperature dependence of elastic constants C_{ij} of $Ba(Fe_{0.963}Co_{0.037})_2As_2$. Where C_{ij} represents C_{11}, C_{33}, C_{44}, $\frac{1}{2}(C_{11} - C_{12})$, and C_{66}.

3.3.3 Temperature dependence of the elastic constants C_{ij} of $Ba(Fe_{0.94}Co_{0.060})_2As_2$.

This composition located near to the QCP in the phase diagram of $Ba(Fe_{1-x}Co_x)_2As_2$. These phase transition temperatures of T_{sc}, T_N, T_S are located closely to each other. For this composition we have studied elastic constants of C_{11}, C_{33}, C_{44}, $\frac{1}{2}(C_{11} - C_{12})$, and C_{66} as shown in Fig. 3.7. Elastic properties of C_{66}, C_{33}, and attenuation α, specific heat and electrical resistivity were studied for two samples of different batch. These results of resistivity and heat capacity were pictured in section one and section two of this chapter.

3.3.4 Temperature dependence of the elastic constants C_{ij} of $Ba(Fe_{0.916}Co_{0.084})_2As_2$.

This sample located in the over doped region of the phase diagram. It shows elastic anomaly at T_{sc}. In this sample C_{66} also shows large elastic softening from room temperature to low temperatures. C_{33} shows step like elastic anomaly at T_{sc}. Other elastic constants show monotonic increase with decreasing temperatures. Results are shown in Fig. 3.8.

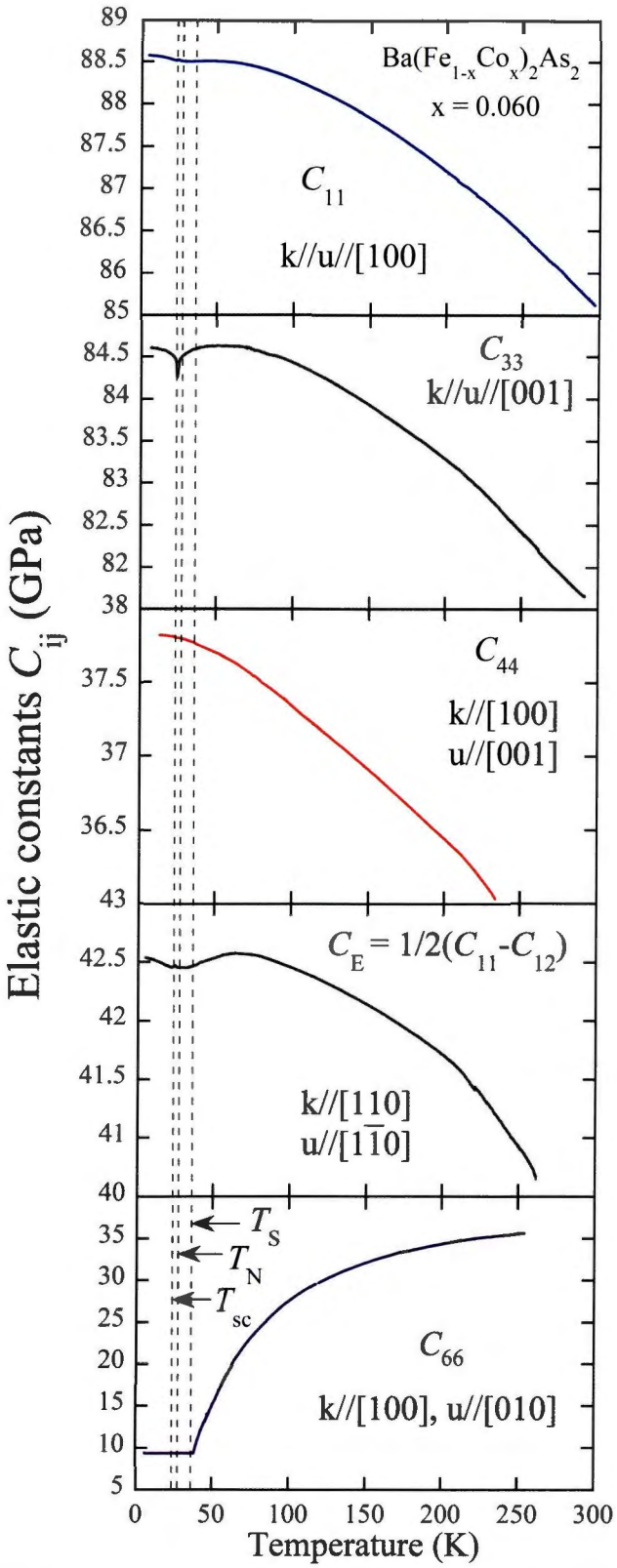

Figure 3.7: Temperature dependence of elastic constants C_{ij} of $Ba(Fe_{0.94}Co_{0.060})_2As_2$. Where C_{ij} representative C_{11}, C_{33}, C_{44}, C_{66}.

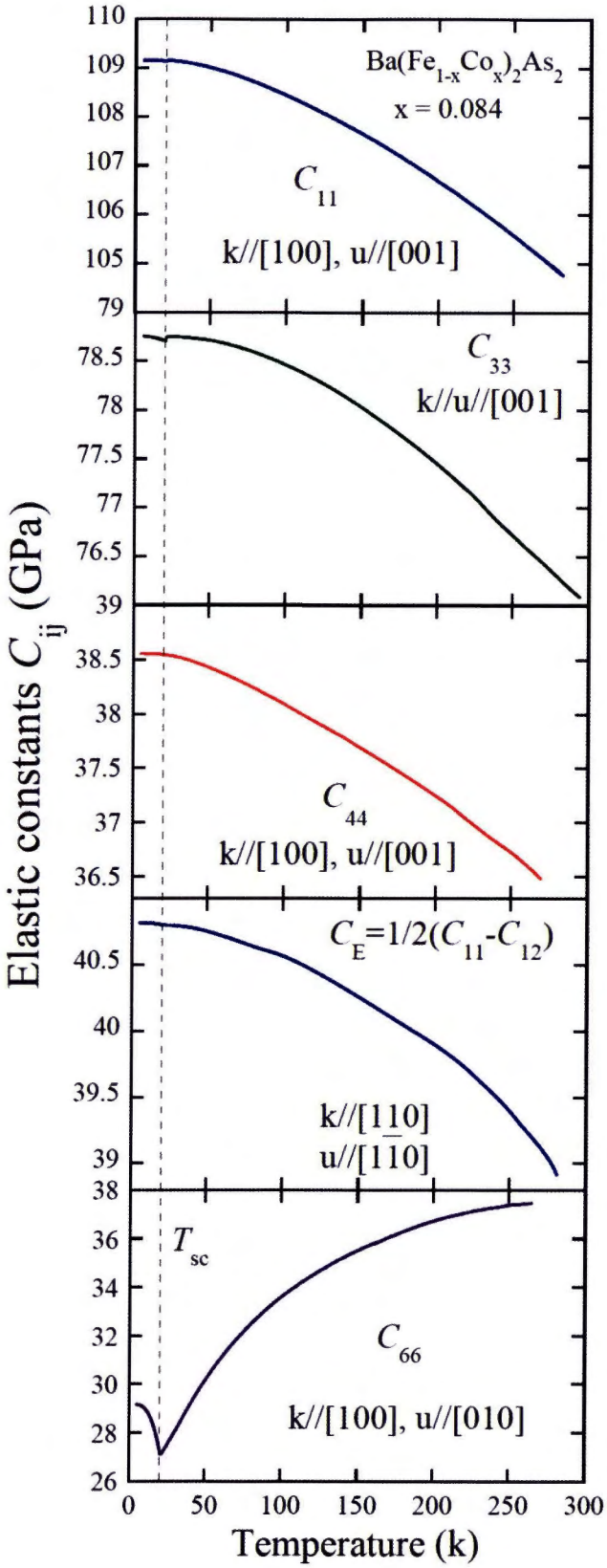

Figure 3.8: Temperature dependence elastic constants C_{ij} of $Ba(Fe_{0.916}Co_{0.084})_2As_2$. Where C_{ij} representative C_{11}, C_{33}, C_{44}, C_{66}.

3.3.5 Temperature dependence of the elastic constants C_{ij} of $Ba(Fe_{0.902}Co_{0.098})_2As_2$.

This sample located in over doped region of the phase diagram of $Ba(Fe_{1-x}Co_x)_2As_2$. This sample shows elastic anomaly at 16.7 K which is corresponds to its superconducting phase transition temperature. In this sample C_{66} also shows large elastic softening from room temperature to low temperatures. C_{33} shows step like elastic anomaly at T_{sc}. Other elastic constants show monotonic increase with decreasing temperatures. Results are shown in Fig. 3.9.

3.3.6 Temperature dependence of the elastic constants C_{ij} of $Ba(Fe_{0.884}Co_{0.116})_2As_2$.

This sample located in over doped region of the phase diagram of $Ba(Fe_{1-x}Co_x)_2As_2$. This sample shows elastic anomaly at around 10 K, it corresponds to its superconducting phase transition temperature of this sample. In this sample C_{66} also shows large elastic softening from room temperature to low temperatures. C_{33} shows step like elastic anomaly at T_{sc}. Other elastic constants show monotonic increase with decreasing temperatures. Results are shown in Fig. 3.10.

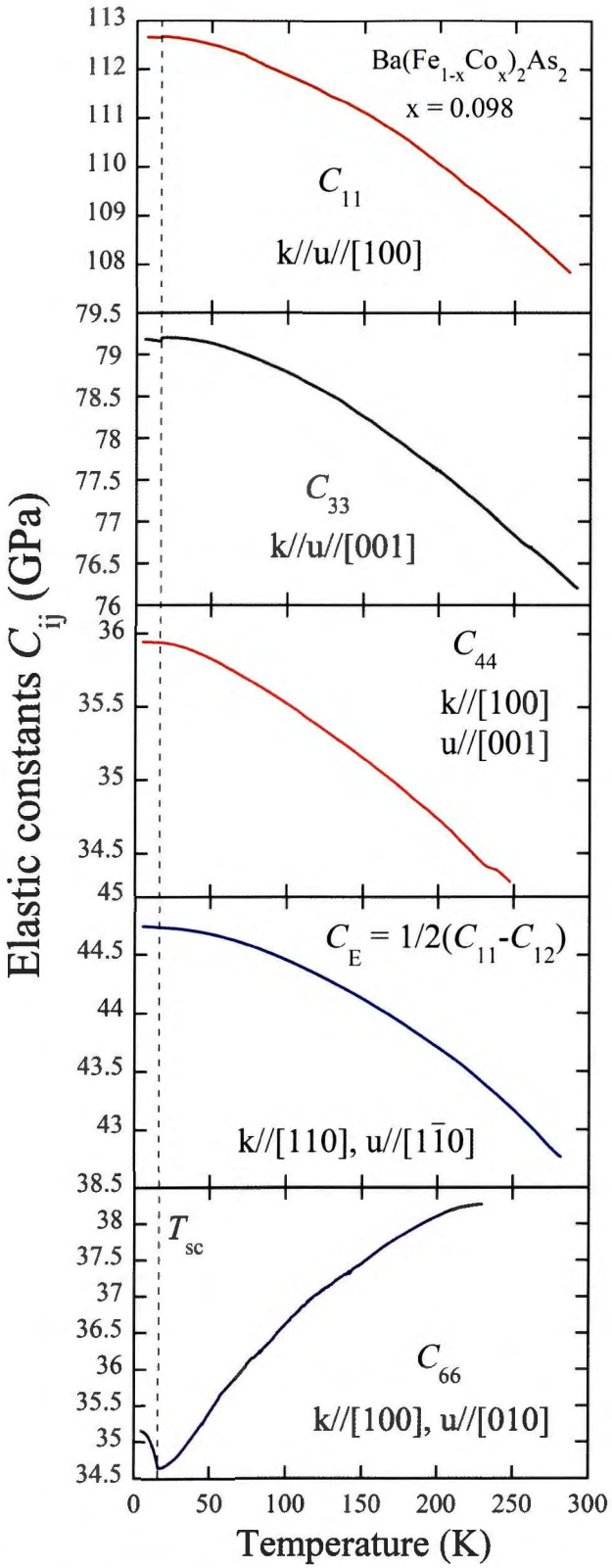

Figure 3.9: Temperature dependence elastic constants C_{ij} of $Ba(Fe_{0.902}Co_{0.098})_2As_2$. Where C_{ij} representative C_{11}, C_{33}, C_{44}, $\frac{1}{2}(C_{11} - C_{12})$, and C_{66} respectively.

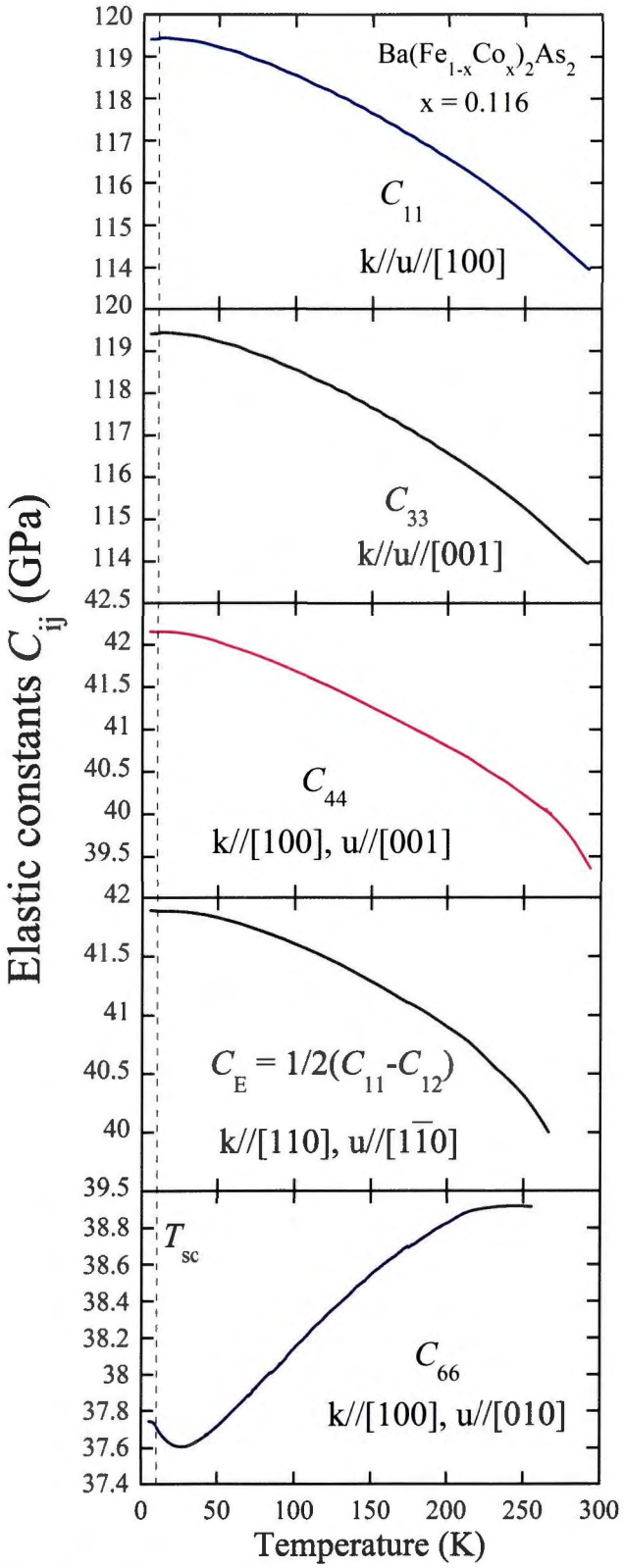

Figure 3.10: Temperature dependence elastic constants C_{ij} of $Ba(Fe_{0.884}Co_{0.116})_2As_2$. Where C_{ij} representative C_{11}, C_{33}, and C_{66} respectively.

3.3.7 Temperature dependence of the elastic constants C_{ij} of $Ba(Fe_{0.839}Co_{0.161})_2As_2$ and $Ba(Fe_{0.755}Co_{0.245})_2As_2$.

As we can see in the phase diagram of $Ba(Fe_{1-x}Co_x)_2As_2$, the Co 16.1% doped and 24.5% doped samples are located far from the QCP, they do not show any phase transitions. Fig. 3.11 and Fig. 3.12 show the temperature dependence of elastic constants of $Ba(Fe_{0.839}Co_{0.161})_2As_2$ and $Ba(Fe_{0.755}Co_{0.245})_2As_2$. All elastic constants show monotonic increase with decreasing temperatures. No elastic anomalies were observed for both samples.

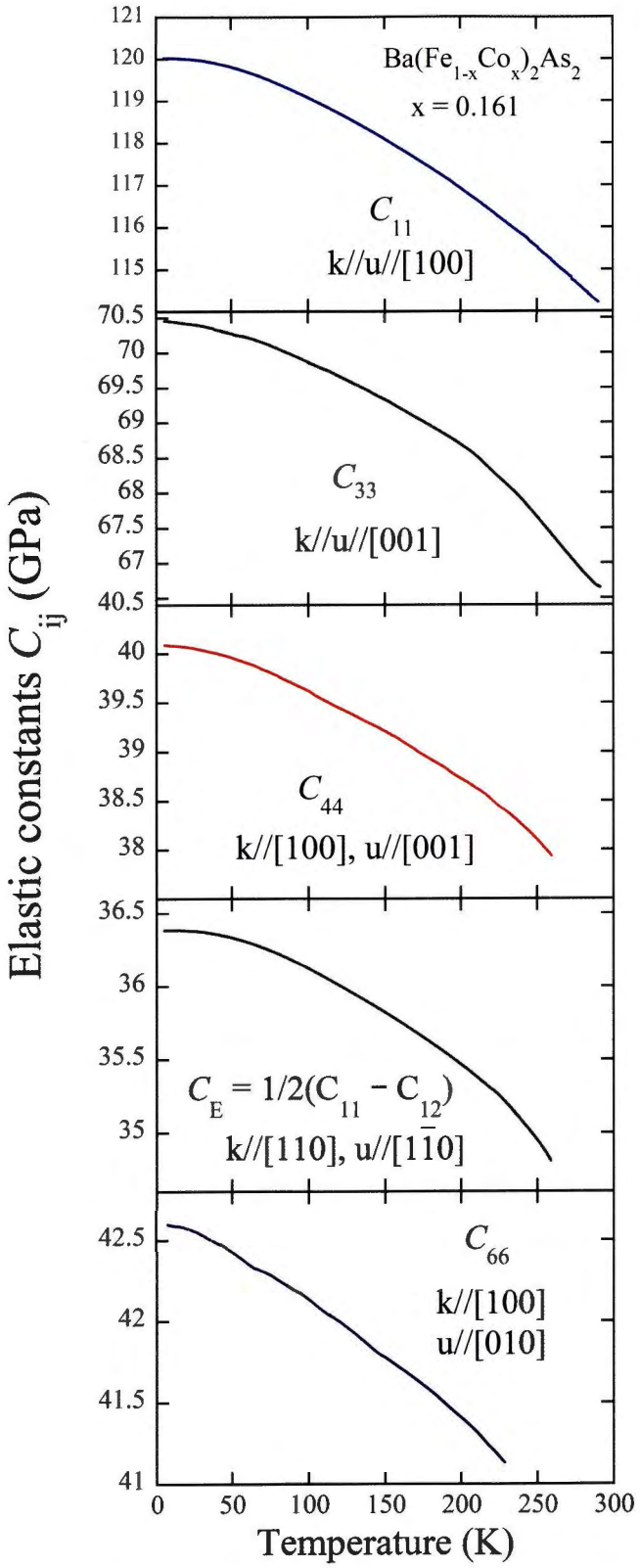

Figure 3.11: Temperature dependence elastic constants C_{ij} of $Ba(Fe_{0.839}Co_{0.161})_2As_2$. Where C_{ij} representative C_{11}, C_{33}, C_{44}, $\frac{1}{2}(C_{11} - C_{12})$, and C_{66} respectively.

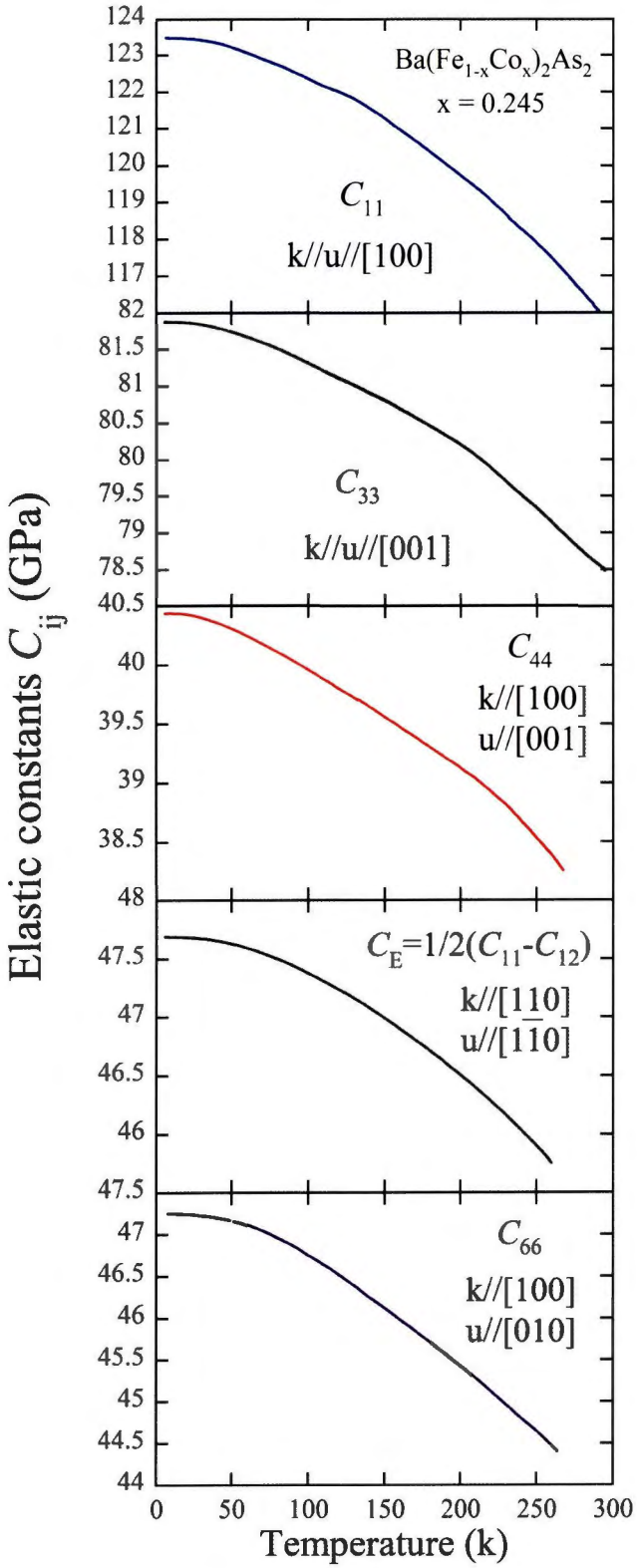

Figure 3.12: Temperature dependence elastic constants C_{ij} of $Ba(Fe_{0.755}Co_{0.245})_2As_2$. Where C_{ij} representative C_{11}, C_{33}, C_{44}, $\frac{1}{2}(C_{11} - C_{12})$, and C_{66} respectively.